Comput Mech (2010) 45:109–125
DOI 10.1007/s00466-009-0422-3

ORIGINAL PAPER

A singular edge-based smoothed finite element method (ES-FEM) for bimaterial interface cracks

L. Chen · G. R. Liu · N. Nourbakhsh-Nia · K. Zeng

Received: 18 May 2009 / Accepted: 20 September 2009 / Published online: 9 October 2009

Abstract The recently developed edge-based smoothed finite element method (ES-FEM) is extended to the mix-mode interface cracks between two dissimilar isotropic materials. The present ES-FEM method uses triangular elements that can be generated automatically for problems even with complicated geometry, and strains are smoothed over the smoothing domains associated with the edges of elements. Considering the stress singularity in the vicinity of the bi-material interface crack tip is of the inverse square root type together with oscillatory nature, a five-node singular crack tip element is devised within the framework of ES-FEM to construct singular shape functions. Such a singular element can be easily implemented since the derivatives of the singular shape term $(1/\sqrt{r})$ are not needed. The mix-mode stress intensity factors can also be easily evaluated by an appropriate treatment during the domain form of the interaction integral. The effectiveness of the present singular ES-FEM is demonstrated via benchmark examples for a wide range of material combinations and boundary conditions.

Keywords Interface crack · Numerical method · Meshfree method · Stress intensity factor · J-integral · Energy release rate · ES-FEM · Singularity

L. Chen (✉) · G. R. Liu · N. Nourbakhsh-Nia
Center for Advanced Computations in Engineering Science (ACES), Department of Mechanical Engineering, National University of Singapore, 9 Engineering Drive 1, Singapore 117576, Singapore
e-mail: g0700888@nus.edu.sg

G. R. Liu
Singapore-MIT Alliance (SMA), E4-04-10, 4 Engineering Drive 3, Singapore 117576, Singapore

K. Zeng
Department of Mechanical Engineering, National University of Singapore, 9 Engineering Drive 1, Singapore 117576, Singapore

1 Introduction

Layered structures are functionally important and can be found in many applications [1], e.g., composite laminates, adhesively bonded joints and thin film/substrate systems. For a layered structure, delamination or interface fracture between two adjacent layers is a typical failure mechanism [2]. Therefore, the development of a robust simulation tool to predict the energy release rate and the stress intensity factors (SIFs) of interface crack in the bimaterial system can lead to a better understanding of the influence of the mismatch in properties and their effects on interface crack growth.

The theoretical foundations for bimaterial interface cracks were studied earlier by Williams [3] and England [4], and further extended by Rice and Sih [5]. For cracks in isotropic and elastic materials, it is well known that the stresses and strains near the crack tip are singular: $\sigma_{ij} \sim 1/\sqrt{r}$, $\varepsilon_{ij} \sim 1/\sqrt{r}$, (where r is the radial distance from the crack tip). However, In the case of a crack lying along a bimaterial interface, the stresses are oscillatory in addition to singularity. Rice [6] introduced a complex **K** for bimaterial interfacial cracks to simulate this feature, in which **K** will be reduced to the classical definition $(K_I,\ K_{II})$ in the absence of mismatch in material properties. The stress singularity in the vicinity of the crack tip of a bimaterial interface crack can be expressed as $r^{-1/2+i\varepsilon}$ [3–6]. However, the oscillatory term $r^{i\varepsilon}$ is in general confined to a small distance close to the crack tip.

The numerical simulation of interface cracks can be carried out with several different approaches. When FEM is used, the eight-node quarter-point element or the six-node quarter-point element (collapsed quadrilateral) is often adopted to model the inverse $\sqrt{r}$ stress singularity in the vicinity of the crack tip [7–9]. Considering the oscillatory singularity of interface crack tip, the stress intensity factors are extracted by an appropriate treatment during the domain

form of the contour interaction integral [10–12]. Recently, Belytschko and Moes developed so-called extended finite element method (XFEM) to model arbitrary discontinuities in meshes [13,14]. This extension exploits the partition of unity property of finite elements, which allows local enrichment functions to be easily incorporated into a finite element approximation while preserving the classical displacement variational setting [15]. Sukumar et al. [16] extended recently the XFEM to bimaterial interface cracks with a modification of enrichment functions. However, the enrichment is only partial in the blending elements at the edge of the enriched sub-domain, and consequently some pathological terms appear in the interpolation, which can destroy the partition of unity property locally.

More recently, Liu et al. [17] have applied the strain smoothing technique to the FEM settings to develop a smoothed finite element method (SFEM) [18,19]. In the SFEM, cell-based strain smoothing technique is incorporated to the standard FEM formulation, so as to reduce the over stiffness of the FEM model. To further reduce the stiffness, a node-based smoothed finite element (NS-FEM) [20] has been formulated using the smoothing domains associated with nodes. The NS-FEM works for triangular, 4-node quadrilateral and even n-sided polygonal elements. When triangular elements are used, the NS-FEM gives the same results as the node-based uniform strain elements [21] or as the LC-PIM (known also as NS-PIM) [22] when the linear shape functions are used for interpolation. The NS-FEM, however, behaves "overly-soft" observed as non-zero energy spurious modes that can lead to temporal instability when it is used to solve the dynamic problems. To reduce this overly-soft behavior, an edge-based smoothed finite element (ES-FEM) was thus invented for both 2D [23] and 3D problems [24]. The ES-FEM uses the triangular mesh that can be generated automatically for problems with complicated geometry, and the strain smoothing domains are associated with the edges of elements. The ES-FEM can properly reduce the softening effects and gives a close-to-exact stiffness, and thus often exhibits super convergence properties, ultra accuracy and high computational efficiency compared to the traditional FEM using the same meshes. Most importantly, the implementation procedure in ES-FEM offers a very convenient way to create the displacement field using the simple point interpolation method (PIM) [25–27]. This is because we need only the shape functions values (not the derivatives) on the edges of the smoothing domains in the ES-FEM formulation in computing the stiffness matrix. Therefore, we can create the $\sqrt{r}$ displacement field using special basis shape functions for interpolation and thus obtain a proper singular stress field in the vicinity of the crack tip.

In this paper, the edge-based smoothed finite element method (ES-FEM) is modified to solve the mix-mode interface cracks between two dissimilar isotropic materials. A five-node singular element is designed within the framework of ES-FEM to construct singular shape functions for the edge-based smoothing domains connected to the crack tip. To model the oscillatory effect $r^{i\varepsilon}$ at the crack tip, the mix-mode stress intensity factors are numerically extracted by the domain form of the interaction integral with appropriate treatments. Intensive benchmark examples show that the present singular ES-FEM improves the accuracy of SIFs and energy release rate in comparison with the standard FEM, the singular FEM and ES-FEM. Excellent agreement between the numerical results and reference solutions with less than 1 percent relative error is achieved for a wide range of material combinations and boundary conditions.

The paper is organized as follows. In Sect. 2, the main ingredients of linear elastic interfacial fracture mechanics are summarized. Section 3 provides a brief description of ES-FEM formulation for bimaterial interface. The construction of the singular shape functions near the interface crack tip is elaborated in Sect. 4. Section 5 discusses the domain interaction integrals for interface crack. In Sect. 6, some numerical examples including different material combinations and boundary conditions are studied to demonstrate the effectiveness of the present method. Some concluding remarks are closed in Sect. 7.

2 Interface fracture mechanics

Figure 1 gives the schematic of a bimaterial interface crack. The crack is located along the interface that is between two semi-infinite planes. Let the plane above the crack be denoted by material 1 with Young's modulus and Poisson's ratio of E_1 and v_1, respectively, and let the plane below the crack be material 2 with corresponding properties of E_2 and v_2. In linear elastic interfacial fracture mechanics [6,28], the complex stress intensity factor $\mathbf{K} = K_I + iK_{II}$ is adopted. The in-plane traction vector at a distance r ahead of the crack takes the form [28]:

$$(\sigma_{yy} + i\tau_{xy})_{\theta=0} = \frac{\mathbf{K} r^{i\varepsilon}}{\sqrt{2\pi r}} \tag{1}$$

where $i = \sqrt{-1}$, and ε is the bimaterial constant which is a function of β, the second Dundurs parameter [29]:

$$\beta = \frac{\mu_1(k_2 - 1) - \mu_2(k_1 - 1)}{\mu_1(k_2 + 1) + \mu_2(k_1 + 1)} \tag{2}$$

$$\varepsilon = \frac{1}{2\pi} \log\left(\frac{1-\beta}{1+\beta}\right) \tag{3}$$

$$k_i = \begin{cases} \dfrac{3 - v_i}{1 + v_i} & \text{(plane stress)} \\ 3 - 4v_i & \text{(plane strain)} \end{cases} \qquad (i = 1, 2) \tag{4}$$

where μ_i, v_i and k_i are the shear modulus, Poisson's ratio and the Kolosov constant, respectively, of material i ($i = 1, 2$).

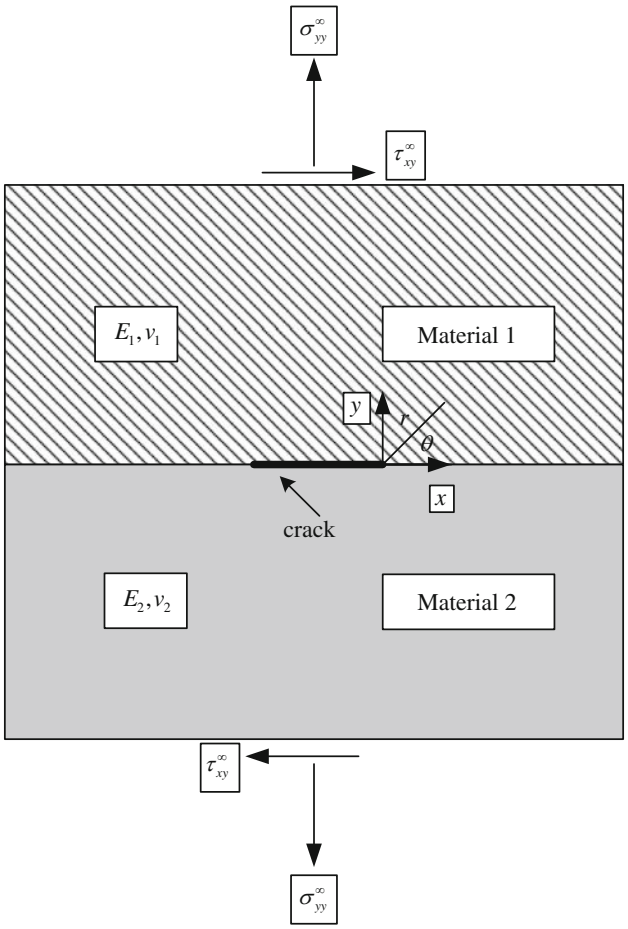

Fig. 1 Bimaterial interface crack

From the above equations, we note that the dimension of $\mathbf{K}$ is [stress][length]$^{1/2-i\varepsilon}$, whereas its amplitude $|\mathbf{K}|$ is the [stress][length]$^{1/2}$. The energy release rate can be related to the stress intensity factor amplitude through the following relation [28].

$$J = G = \frac{1}{E^*}\frac{|\mathbf{K}|^2}{\cosh^2(\pi\varepsilon)}, \quad |\mathbf{K}|^2 = \mathbf{K}\bar{\mathbf{K}} = K_I^2 + K_{II}^2 \tag{5}$$

where

$$\frac{2}{E^*} = \frac{1}{\bar{E}_1} + \frac{1}{\bar{E}_2}, \quad \bar{E}_i = \begin{cases} E_i & \text{(plane stress)} \\ \frac{E_i}{1-\nu_i^2} & \text{(plane strain)} \end{cases} \tag{6}$$

The phase angle ψ is a measure of the relative proportion of shear to normal tractions at a characteristic distance l ahead of the crack tip. It is defined through the relation [6].

$$\mathbf{K}l^{i\varepsilon} = |\mathbf{K}|\, \mathrm{e}^{i\psi} \tag{7}$$

or

$$\psi = \tan^{-1}\left(\frac{\mathrm{Im}[\mathbf{K}l^{i\varepsilon}]}{\mathrm{Re}[\mathbf{K}l^{i\varepsilon}]}\right) \tag{8}$$

The phase angle ψ is an important parameter in the characterization of interfacial fracture toughness, and the characteristic length l associated with a factor of 10 change affects little the phase angle for the small ε [6]. Therefore, in reporting the phase angle for a given loading configuration, the characteristic length l can be taken as the crack (ligament) length or a specimen dimension. It is apparent from the above discussion that, unlike the treatment of cracks in isotropic materials, tension and shear effects are inseparable in the vicinity of interface crack tip.

The Cartesian components of the near-tip asymptotic displacement fields can be obtained from Reference [6]. The crack-tip displacement fields in the upper-half plane (replace $\varepsilon\pi$ by $-\varepsilon\pi$ for the lower-half plane) are [28]:

$$u_j = \frac{1}{2\mu_1}\sqrt{\frac{r}{2\pi}}\left\{\mathrm{Re}[\mathbf{K}l^{i\varepsilon}]\tilde{u}_j^I(\theta,\varepsilon,\nu_1) + \mathrm{Im}[\mathbf{K}l^{i\varepsilon}]\tilde{u}_j^{II}(\theta,\varepsilon,\nu_1)\right\} \ (j = x \text{ or } y) \tag{9}$$

$$\tilde{u}_x^I = A\left[-e^{2\varepsilon(\pi-\theta)}\left(\cos\frac{\theta}{2} + 2\varepsilon\sin\frac{\theta}{2}\right) + k_1\left(\cos\frac{\theta}{2} - 2\varepsilon\sin\frac{\theta}{2}\right) + (1+4\varepsilon^2)\sin\frac{\theta}{2}\sin\theta\right] \tag{10}$$

$$\tilde{u}_x^{II} = A\left[e^{2\varepsilon(\pi-\theta)}\left(\sin\frac{\theta}{2} - 2\varepsilon\cos\frac{\theta}{2}\right) + k_1\left(\sin\frac{\theta}{2} + 2\varepsilon\cos\frac{\theta}{2}\right) + (1+4\varepsilon^2)\cos\frac{\theta}{2}\sin\theta\right] \tag{11}$$

$$\tilde{u}_y^I = A\left[e^{2\varepsilon(\pi-\theta)}\left(\sin\frac{\theta}{2} - 2\varepsilon\cos\frac{\theta}{2}\right) + k_1\left(\sin\frac{\theta}{2} + 2\varepsilon\cos\frac{\theta}{2}\right) - (1+4\varepsilon^2)\cos\frac{\theta}{2}\sin\theta\right] \tag{12}$$

$$\tilde{u}_y^{II} = A\left[e^{2\varepsilon(\pi-\theta)}\left(\cos\frac{\theta}{2} + 2\varepsilon\sin\frac{\theta}{2}\right) - k_1\left(\cos\frac{\theta}{2} - 2\varepsilon\sin\frac{\theta}{2}\right) + (1+4\varepsilon^2)\sin\frac{\theta}{2}\sin\theta\right] \tag{13}$$

where

$$A = \frac{e^{-\varepsilon(\pi-\theta)}}{(1+4\varepsilon^2)\cosh(\pi\varepsilon)} \tag{14}$$

and (r,θ) are polar co-ordinates with origin at the right crack tip.

In Eq. (9), Re[·] and Im[·] denote the real and imaginary parts of a complex number, respectively, and $r^{i\varepsilon} = \mathrm{e}^{i\varepsilon\log r} = \cos(\varepsilon\log r) + i\sin(\varepsilon\log r)$.

3 ES-FEM for bimaterial interface

3.1 Governing equations

Consider a 2D static elastic problem governed by the equilibrium equation in the domain $\Omega = \Omega^+ + \Omega^-$ separated by a single interface, Γ_i, as shown in Fig. 2:

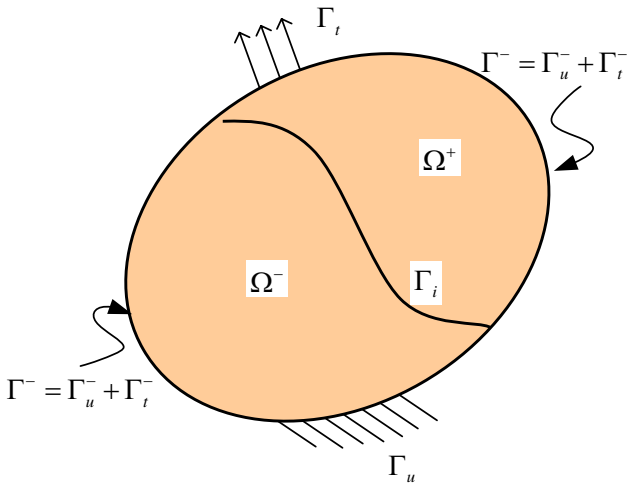

Fig. 2 Inhomogeneous body with interface subjected loads

$$\nabla \cdot \boldsymbol{\sigma} + \mathbf{b} = 0 \text{ in } \Omega \tag{15}$$

where ∇ is the divergence operator, $\boldsymbol{\sigma}$ is the Cauchy stress tensor and $\mathbf{b}$ is the body force term.

The essential and natural boundary conditions are given by:

$$\mathbf{u} = \mathbf{u}_\Gamma \quad \text{on } \Gamma_u \tag{16}$$

$$\boldsymbol{\sigma}\mathbf{n} = \mathbf{t}_\Gamma \quad \text{on } \Gamma_t \tag{17}$$

where $\mathbf{u}_\Gamma$ and $\mathbf{t}_\Gamma$ are the vectors of the prescribed displacements and tractions respectively, and $\mathbf{n}$ is the outward normal unit vector defined on the boundary Γ.

On the interface, Γ_i, continuity of tractions and displacements requires

$$[\![t_i]\!] = t_i^+ - t_i^- = 0 \tag{18}$$

$$[\![u_i]\!] = u_i^+ - u_i^- = 0 \tag{19}$$

where $[\![.]\!]$ denotes a jump.

The constitution equation (stress–strain relation) is given by:

$$\boldsymbol{\sigma} = \mathbf{D}\boldsymbol{\varepsilon} \tag{20}$$

where $\mathbf{D}$ is the matrix of material constants, and $\boldsymbol{\sigma}^T = \{\sigma_{xx}\ \sigma_{yy}\ \tau_{xy}\}$ and $\boldsymbol{\varepsilon}^T = \{\varepsilon_{xx}\ \varepsilon_{yy}\ \gamma_{xy}\}$ are the vector forms of the stress and strain tensor respectively.

3.2 Edge-based strain smoothing

The domain Ω is first discretized into N_e of non-overlapping and non-gap elements and N_n nodes. Then, the approximation of displacement field for a 2D static elasticity problem is given by:

$$\mathbf{u}(\mathbf{x}) = \sum_{i \in n_n^e} \mathbf{N}_i(\mathbf{x})\mathbf{d}_i \tag{21}$$

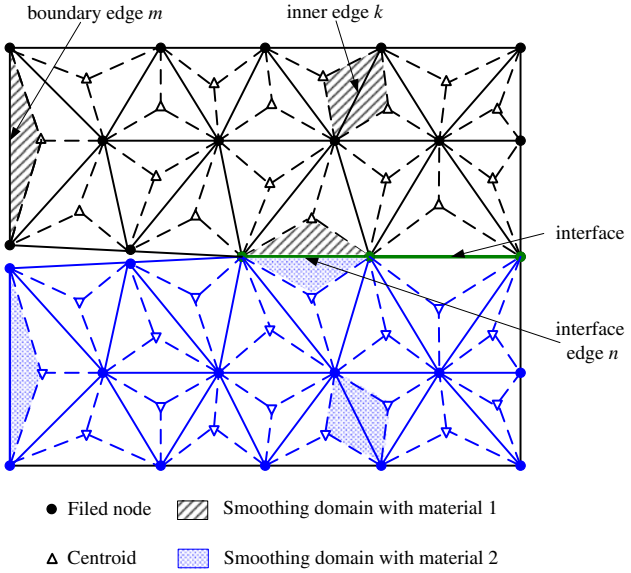

Fig. 3 Construction of edge-based strain smoothing domains

where $\mathbf{u} = \{u_x\ u_y\}^T$ is the vector of the displacement, respectively, in x-axis and y-axis, n_n^e is the set of nodes of the element containing $\mathbf{x} = \{x\ y\}^T$, $\mathbf{d}_i = \{d_{xi}\ d_{yi}\}^T$ is the vector of nodal displacements, and $\mathbf{N}_i$ is a matrix of shape functions

$$\mathbf{N}_i(\mathbf{x}) = \begin{bmatrix} N_i(\mathbf{x}) & 0 \\ 0 & N_i(\mathbf{x}) \end{bmatrix} \tag{22}$$

in which $N_i(\mathbf{x})$ is the shape function for node i.

The compatibility equation (strain-displacement relation) is given by:

$$\boldsymbol{\varepsilon} = \nabla_s \mathbf{u} \tag{23}$$

where $\nabla_s \mathbf{u}$ is the symmetric gradient of the displacement field.

In the ES-FEM, however, we do not use the compatible strains $\boldsymbol{\varepsilon} = \nabla_s \mathbf{u}$ but the strains "smoothed" over the local smoothing domains. These local smoothing domains are constructed with respect to the edges of triangular elements such that $\Omega = \cup_{k=1}^{N_s} \Omega_k^s$ and $\Omega_i^s \cap \Omega_j^s = 0, \forall i \neq j$, in which N_s is the number of smoothing domains. The rule is that the problem domain is first divided into two sub-domains based on the assignment of materials as shown in Fig. 3. Then, for each sub-domain with the isotropic material, the smoothing domain corresponding to the inner edge k, Ω_k^s, is formed by connecting two end points of edge k and two centroids of the adjacent triangular elements. The smoothing domain for the boundary edge m or the interface edge n, Ω_m^s or Ω_n^s, is just one third region of triangular element which contains the edge m or the edge n.

Using the edge-based smoothing domains, *smoothed* strains can be obtained using the *compatible* strains $\boldsymbol{\varepsilon} = \nabla_s \mathbf{u}$

through the following smoothing operation over domain Ω_k^s associated with the edge k:

$$\bar{\boldsymbol{\varepsilon}}_k = \frac{1}{A_k^s}\int_{\Omega_k^s} \nabla_s \mathbf{u}(\mathbf{x}) d\Omega = \frac{1}{A_k^s}\int_{\Gamma_k^s} \mathbf{L}_n \mathbf{u}(\mathbf{x}) d\Gamma \tag{24}$$

where $A_k^s = \int_{\Omega_k^s} d\Omega$ is the area of the smoothing domain Ω_k^s, Γ_k^s is the boundary of the smoothing domain and $\mathbf{L}_n$ is the outward unit normal matrix which can be expressed as:

$$\mathbf{L}_n = \begin{bmatrix} n_x & 0 \\ 0 & n_y \\ n_y & n_x \end{bmatrix} \tag{25}$$

Substituting Eq. (21) into Eq. (24), the smoothed strain can be written in the following matrix form of nodal displacements.

$$\bar{\boldsymbol{\varepsilon}}_k = \sum_{i \in n_k^s} \bar{\mathbf{B}}_i(\mathbf{x}_k)\bar{\mathbf{d}}_i \tag{26}$$

where n_k^s is the set of nodes associated the smoothing domain Ω_k^s; and $\bar{\mathbf{B}}_i(\mathbf{x}_k)$ is termed as the smoothed strain gradient matrix that is calculated by:

$$\bar{\mathbf{B}}_i(\mathbf{x}_k) = \begin{bmatrix} \bar{b}_{ix}(\mathbf{x}_k) & 0 \\ 0 & \bar{b}_{iy}(\mathbf{x}_k) \\ \bar{b}_{iy}(\mathbf{x}_k) & \bar{b}_{ix}(\mathbf{x}_k) \end{bmatrix} \tag{27}$$

where $\bar{b}_{ih}(\mathbf{x}_k)$, $h = x,\ y$, is computed by:

$$\bar{b}_{ih}(\mathbf{x}_k) = \frac{1}{A_k^s}\int_{\Gamma_k^s} n_h(\mathbf{x}) N_i(\mathbf{x}) d\Gamma \tag{28}$$

Using the Gauss integration along the segments of boundary Γ_k^s, we have:

$$\bar{b}_{ih} = \frac{1}{A_k^s}\sum_{m=1}^{N_{seg}} \left[\sum_{n=1}^{N_{gau}} w_{m,n} N_i\left(\mathbf{x}_{m,n}\right) n_h\left(\mathbf{x}_{m,n}\right) \right] \quad (h = x,\ y) \tag{29}$$

where N_{seg} is the number of segments of the boundary Γ_k^s, N_{gau} is the number of Gauss points used in each segment, $w_{m,n}$ is the corresponding weight of Gauss points, n_h is the outward unit normal corresponding to each segment on the smoothing domain boundary and $\mathbf{x}_{m,n}$ is the nth Gaussian point on the mth segment of the boundary Γ_k^s.

3.3 Discretized system equation

The discrete equations of ES-FEM are generated from the smoothed Galerkin weak form:

$$\int_\Omega \delta\left(\bar{\boldsymbol{\varepsilon}}(\mathbf{u})\right)^T \mathbf{D}\left(\bar{\boldsymbol{\varepsilon}}(\mathbf{u})\right) d\Omega - \int_\Omega \delta\mathbf{u}^T \mathbf{b} d\Omega - \int_{\Gamma_t} \delta\mathbf{u}^T \mathbf{t}_\Gamma d\Gamma = 0 \tag{30}$$

Substituting the approximated displacements in Eq. (21) and the smoothed strains from Eq. (24) into the smoothed Galerkin weak form, and invoking the arbitrary nature of the variation operations, a set of discretized algebraic system equations can be obtained in the following matrix form:

$$\bar{\mathbf{K}}\bar{\mathbf{d}} = \mathbf{f} \tag{31}$$

where $\bar{\mathbf{d}}$ is the displacement vector of all the nodes, $\bar{\mathbf{K}}$ is the global stiffness matrix and $\mathbf{f}$ is the nodal force vector that can be obtained by:

$$\mathbf{f} = \int_\Omega N^T(\mathbf{x})\mathbf{b} d\Omega + \int_{\Gamma_t} N^T(\mathbf{x})\mathbf{t}_\Gamma d\Gamma \tag{32}$$

The entries in sub-matrices of the stiffness matrix $\bar{\mathbf{K}}$ in Eq. (31) can then be expressed as:

$$\bar{\mathbf{K}}_{ij} = \sum_{k=1}^{N_s} \bar{\mathbf{K}}_{ij,k}^s \tag{33}$$

where the summation means an assembly process, and $\bar{\mathbf{K}}_{ij,k}^s$ is the stiffness matrix associated with the smoothing domain Ω_k^s and can be computed by:

$$\bar{\mathbf{K}}_{ij,k}^s = \int_{\Omega_k^s} \bar{\mathbf{B}}_i^T \mathbf{D} \bar{\mathbf{B}}_j d\Omega = \sum_{k=1}^{N_s} \bar{\mathbf{B}}_i^T \mathbf{D} \bar{\mathbf{B}}_j A_k^s \tag{34}$$

4 Construction of singularity of interface crack tip

A fundamental issue when modeling linear interface fracture mechanics problems is to simulate the singularity of stress field near the interface crack tip. However, since the stress singularity at the crack tip of a bimaterial interface crack is of the inverse square root type, the polynomial basis shape functions can not represent the stress and strain field near the crack tip. In the other hand, only the shape functions values (not the derivatives) on the edges of the smoothing domains in the ES-FEM formulation are needed to compute the stiffness matrix. Therefore, we can create the $\sqrt{r}$ displacement field using special basis shape functions for interpolation and thus obtain a $1/\sqrt{r}$ singular stress field in the vicinity of the crack tip.

In this work, a five-node singular element containing the crack tip is specially designed within the framework of ES-FEM to construct special basis (singular) shape functions. As shown in Fig. 4, one node is added to each edge of the triangular elements connected to the crack tip. The location of the added node is at the one quarter length of the edge from the crack tip. Based on this setting, a field function $u(\mathbf{x})$

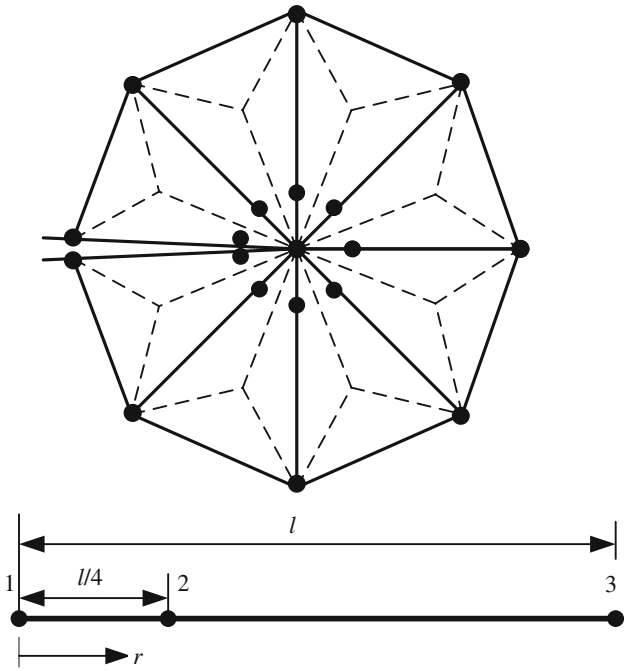

Fig. 4 Node arrangement near the crack tip. *Dashed lines* construct the edge-based smoothing domains directly connected to the crack tip node

at any point of interest on an edge of a singular element can be constructed by the three nodes along the edge:

$$u(\mathbf{x}) = \sum_{i=1}^{3} p_i(\mathbf{x}) a_i = a_0 + a_1 r + a_2 \sqrt{r} \tag{35}$$

where r is the radial coordinate originated at the crack-tip, and a_i is the interpolation coefficient for $p_i(\mathbf{x})$ corresponding to the given point $\mathbf{x}$. The coefficients a_i in Eq. (35) can be determined by enforcing Eq. (35) to exactly pass through nodal values of the three nodes along the edge:

$$u_1 = a_0 + a_1 r_1 + a_2 \sqrt{r_1} \tag{36}$$

$$u_2 = a_0 + a_1 r_2 + a_2 \sqrt{r_2} \tag{37}$$

$$u_3 = a_0 + a_1 r_3 + a_2 \sqrt{r_3} \tag{38}$$

Solving this simultaneous system of three equations for a_i, and substituting them back to Eq. (35), we shall obtain:

$$u(\mathbf{x}) = \begin{bmatrix} \underbrace{1+2\frac{r}{l}-3\sqrt{\frac{r}{l}}}_{\phi_1} & \underbrace{-4\frac{r}{l}+\sqrt{\frac{r}{l}}}_{\phi_2} & \underbrace{2\frac{r}{l}-\sqrt{\frac{r}{l}}}_{\phi_3} \end{bmatrix} \begin{Bmatrix} u_1 \\ u_2 \\ u_3 \end{Bmatrix} \tag{39}$$

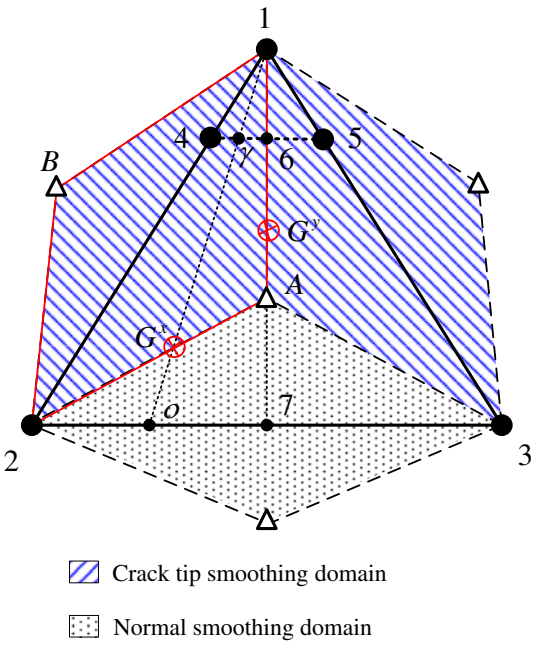

Fig. 5 The schematic of five-node element

where l is the length of the element edge, and ϕ_i $(i = 1, 2, 3)$ are the shape functions for these three nodes on the edge that can be written:

$$\begin{cases} \phi_1 = 1 + 2\frac{r}{l} - 3\sqrt{\frac{r}{l}} \\ \phi_2 = -4\frac{r}{l} + \sqrt{\frac{r}{l}} \\ \phi_3 = 2\frac{r}{l} - \sqrt{\frac{r}{l}} \end{cases} \tag{40}$$

Figure 5 shows a five-node element connected to the node of crack tip. From the figure, we can see that each five-node element is constructed by three edge-based smoothing domains: two are the crack tip smoothing domains and one is normal smoothing domain. To perform the point interpolation within the crack tip smoothing domain, it is assumed that the field function u varies in the same way as given in Eq. (35) in the radial direction. In the tangential direction, however, it is assumed to vary linearly. For points 6 and 7 which are the midpoints of lines 2–3 and 4–5, the field functions can be evaluated simply as follows.

$$u_6 = \frac{1}{2}(u_2 + u_3) \tag{41}$$

$$u_7 = \frac{1}{2}(u_4 + u_5) \tag{42}$$

Remind that in the formulation of ES-FEM, to compute the smoothed strain gradient matrix $\bar{\mathbf{B}}_i(\mathbf{x}_k)$ by Eqs. (27) and (29), only the shape function values at the Gauss points along the boundary segments are needed. This is also performed similarly to the present singular ES-FEM. However, in the standard ES-FEM using only normal smoothing domains, the

shape function used is always linear compatible along any boundary segments, only one Gauss point is needed on each boundary segment. In the present singular ES-FEM which uses both the crack tip smoothing domain and the normal smoothing domain, a proper number of Gauss points hence need to be used on the boundary segments of the crack tip smoothing domain, which depend on the order of the assumed displacement field (or shape function) along these boundary segments. The displacement in the vicinity of the crack tip possesses the $\sqrt{r}$ behavior near the crack tip, and thus more Gauss points need to be used for the segments of the crack tip smoothing domain to ensure the accuracy.

Specifically as shown in Fig. 5, for the crack tip smoothing domain filled with the blue shadow surrounded by the set of boundary segments of 1A-A2-2B-B1, there are two kinds of segments: (1) one is nearly along the tangential direction (A2 and 2B); (2) another is along the radial direction (1A and B1).

We now construct specifically the shape function for Gauss points on two kinds of boundary segments.

(i) For the Gauss point G^x on a segment nearly along the tangential direction (for example A2, this point is also on the line $1-\gamma-o$ as shown in Fig. 5), the field function is interpolated as:

$$u = u_1\phi_1 + u_\gamma\phi_2 + u_o\phi_3 \tag{43}$$

where

$$u_\gamma = \left(1 - \frac{l_{\gamma-4}}{l_{4-5}}\right)u_4 + \frac{l_{\gamma-4}}{l_{4-5}}u_5 \tag{44}$$

$$u_o = \left(1 - \frac{l_{o-2}}{l_{2-3}}\right)u_2 + \frac{l_{o-2}}{l_{2-3}}u_3 \tag{45}$$

in which l_{i-j} is the distance between points i and j. Because the simple fact that $\frac{l_{\gamma-4}}{l_{4-5}} = \frac{l_{o-4}}{l_{2-3}} = \eta$ we finally arrive at

$$\begin{aligned} u = {} & \underbrace{\phi_1}_{N_1}u_1 + \underbrace{(1-\eta)\phi_3}_{N_2}u_2 + \underbrace{\eta\phi_3}_{N_3}u_3 \\ & + \underbrace{(1-\eta)\phi_2}_{N_4}u_4 + \underbrace{\eta\phi_2}_{N_5}u_5 \end{aligned} \tag{46}$$

(ii) For the Gauss point G^y on the segment of 1A along the radial direction as shown in Fig. 5, the field function is interpolated as:

$$\begin{aligned} u = {} & u_1\phi_1 + u_5\phi_2 + u_3\phi_3 = \phi_1 u_1 + 0\times u_2 + \phi_3 u_3 \\ & + 0\times u_4 + \phi_2 u_5 \end{aligned} \tag{47}$$

By comparison of Eqs. (46) and (47), we can easily find that Eq. (47) is just one case of Eq. (46) for $\eta = 1$. Thus, the general form of shape functions for the interpolation at any point within the five-node crack-tip element can be written as:

$$\begin{cases} N_1 = 1 + 2\frac{r}{l} - 3\sqrt{\frac{r}{l}} \\ N_2 = (1-\eta)\left(2\frac{r}{l} - \sqrt{\frac{r}{l}}\right) \\ N_3 = \eta\left(2\frac{r}{l} - \sqrt{\frac{r}{l}}\right) \\ N_4 = (1-\eta)\left(-4\frac{r}{l} + \sqrt{\frac{r}{l}}\right) \\ N_5 = \eta\left(-4\frac{r}{l} + \sqrt{\frac{r}{l}}\right) \end{cases} \tag{48}$$

It is clear that the shape functions are (complete) linear in r and "enriched" with $\sqrt{r}$ that is capable to produce a strain (hence stress) singularity field of an order of $^1/_2$ near the crack-tip. This is because the strain is evaluated from the derivatives of the assumed displacements.

It is also noted that since the derivatives of the singular shape term $(1/\sqrt{r})$ are not required to calculate the system stiffness matrix, the formulation of the present five-node element is much simply. Moreover, it does not need to use the quadratic elements. Therefore, it can be very easily incorporated into the standard ES-FEM.

5 Domain interaction integral methods for bimaterial interface cracks

In the linear elasticity, the general form of J-contour integral, which is identical to the energy release rate G, for a two dimensional crack can be written as [30]:

$$J = G = \int_\Gamma \left(\frac{1}{2}\sigma_{ik}\varepsilon_{ik}\delta_{xj} - \sigma_{ij}u_{i,x}\right)n_j d\Gamma, \quad \begin{matrix} i = x \text{ or } y; \\ j = x \text{ or } y \end{matrix} \tag{49}$$

The J-integral remains globally path independent for bimaterial interface crack problems when there exists no material inhomogeneity in the direction parallel to the crack [30]. In this case, the mixed-mode stress intensity factors K_I and K_{II} can be readily evaluated using the domain form [31] of the contour interaction integral [10].

In the interaction integral method [10,14], two states of a cracked body are used to evaluate the stress intensity factors. State 1, $(\sigma_{ij}^{(1)}, \varepsilon_{ij}^{(1)}, u_i^{(1)})$, corresponds to the present state and state 2, $(\sigma_{ij}^{(2)}, \varepsilon_{ij}^{(2)}, u_i^{(2)})$, is an auxiliary state. Here, unlike the cracks in homogeneous materials, it is chosen as the asymptotic fields with the oscillatory effect $r^{i\varepsilon}$ at interface crack tip. On summing the J-integral of two states, we can obtain the contour interaction integral [14]:

$$I=\int_{\Gamma}(\sigma_{ik}^{(1)}\varepsilon_{ik}^{(2)}\delta_{xj}-\sigma_{ij}^{(1)}u_{i,x}^{(2)}-\sigma_{ij}^{(2)}u_{i,x}^{(1)})n_j d\Gamma,\quad k=x \text{ or } y \tag{50}$$

From Eq. (5), the interaction integral is related to the SIFs through the relation [14].

$$I=\frac{2}{E^*}\frac{K_I^{(1)}K_I^{(2)}+K_{II}^{(1)}K_{II}^{(2)}}{\cosh^2(\pi\varepsilon)} \tag{51}$$

Making the judicious choice of state 2 (auxiliary) as the pure Mode I asymptotic fields, i.e., setting $K_I^{(2)}=1$, $K_I^{(2)}=0$ and evaluating $I=I_I$, we can compute K_I and we proceed in an analogous manner to evaluate K_{II}:

$$K_I=\frac{E^*\cosh^2(\pi\varepsilon)}{2}I_I\quad K_{II}=\frac{E^*\cosh^2(\pi\varepsilon)}{2}I_{II} \tag{52}$$

To extract the mixed-mode stress intensity factors K_I and K_{II} for bimaterial interface cracks, the auxiliary displacement field in the local $x-y$ crack-tip co-ordinate system (Fig. 1) is more complex compared to the cracks in homogeneous materials, and can be written as:

$$u_j=\begin{cases}\frac{1}{4\mu_1\cosh(\pi\varepsilon)}\sqrt{\frac{r}{2\pi}}f_j(r,\theta,\varepsilon,k_1)(\text{upper-half plane})\\ \frac{1}{4\mu_2\cosh(\pi\varepsilon)}\sqrt{\frac{r}{2\pi}}f_j(r,\theta,\varepsilon,k_2)(\text{lower-half plane})\end{cases}\quad j=x \text{ or } y \tag{53}$$

where ε is the bimaterial constant that is defined in Eq. (3), and μ_i, k_i are the shear modulus and the Kolosov constant, respectively, of material i ($i=1,2$).

To extract K_I, the functions f_x and f_y are

$$f_x=D+T_1,\quad f_y=-C-T_2 \tag{54}$$

whereas to compute K_{II}, the expressions for f_x and f_y are:

$$f_x=-C+T_2,\quad f_y=-D+T_1 \tag{55}$$

In the above equations δ, φ, C, D, T_1 and T_2 are defined as:

$$C=\beta'\gamma\cos\frac{\theta}{2}-\beta\gamma'\sin\frac{\theta}{2},\quad D=\beta\gamma\cos\frac{\theta}{2}+\beta'\gamma'\sin\frac{\theta}{2} \tag{56}$$

$$T_1=2\delta\sin\theta\sin\varphi,\quad T_2=2\delta\sin\theta\cos\varphi \tag{57}$$

$$\delta=\begin{cases}e^{-(\pi-\theta)\varepsilon}(\text{upper-half plane})\\ e^{(\pi+\theta)\varepsilon}(\text{lower-half plane})\end{cases}\quad \varphi=\varepsilon\log r+\frac{\theta}{2} \tag{58}$$

$$\beta=\frac{0.5\cos(\varepsilon\log r)+\varepsilon\sin(\varepsilon\log r)}{0.25+\varepsilon^2},\quad \beta'=\frac{0.5\sin(\varepsilon\log r)-\varepsilon\cos(\varepsilon\log r)}{0.25+\varepsilon^2} \tag{59}$$

$$\gamma=k\delta-\frac{1}{\delta},\ \gamma'=k\delta+\frac{1}{\delta},\quad k=\begin{cases}k_1\ (\text{upper-half plane})\\ k_2\ (\text{lower-half plane})\end{cases} \tag{60}$$

The auxiliary strain components are the symmetric gradient of the auxiliary displacement components:

$$\varepsilon_{ij}^{(2)}=\frac{1}{2}(u_{i,j}^{(2)}+u_{j,i}^{(2)}),\quad i=x \text{ or } y;\quad j=x \text{ or } y \tag{61}$$

On defining

$$E=\beta'\gamma'\cos\frac{\theta}{2}-\beta\gamma\sin\frac{\theta}{2},\quad F=\beta\gamma'\cos\frac{\theta}{2}+\beta'\gamma\sin\frac{\theta}{2} \tag{62}$$

we have

$$C_{,r}=\frac{\varepsilon D}{r},\quad C_{,\theta}=-\frac{F}{2}+\varepsilon E \tag{63}$$

$$D_{,r}=-\frac{\varepsilon C}{r},\quad D_{,\theta}=\frac{E}{2}+\varepsilon F \tag{64}$$

On setting

$$T_3=2\delta\cos\theta\sin\varphi,\quad T_4=2\delta\cos\theta\cos\varphi \tag{65}$$

we have

$$T_{1,r}=\frac{\varepsilon T_2}{r},\quad T_{1,\theta}=\varepsilon T_1+\frac{T_2}{2}+T_3 \tag{66}$$

$$T_{2,r}=\frac{\varepsilon T_1}{r},\quad T_{2,\theta}=\varepsilon T_2-\frac{T_1}{2}+T_4 \tag{67}$$

If K_I is to be extracted, then

$$f_{x,\alpha}=D_{,\alpha}+T_{1,\alpha},\quad f_{y,\alpha}=-C_{,\alpha}-T_{2,\alpha}\quad(\alpha=r,\theta) \tag{68}$$

whereas if K_{II} is to be computed, then

$$f_{x,\alpha}=-C_{,\alpha}+T_{2,\alpha},\quad f_{y,\alpha}=-D_{,\alpha}-T_{1,\alpha}\quad(\alpha=r,\theta) \tag{69}$$

Since $r_{,x}=\cos\theta$, $r_{,y}=\sin\theta$, $\theta_{,x}=-\sin\theta/r$ and $\theta_{,y}=\cos\theta/r$, on using the chain rule, we can write the derivatives of f_x and f_y in the $x-y$ co-ordinate system as:

$$f_{x,x}=f_{x,r}r_{,x}+f_{x,\theta}\theta_{,x},\quad f_{x,y}=f_{x,r}r_{,y}+f_{x,\theta}\theta_{,y} \tag{70}$$

$$f_{y,x}=f_{y,r}r_{,x}+f_{y,\theta}\theta_{,x},\quad f_{y,y}=f_{y,r}r_{,y}+f_{y,\theta}\theta_{,y} \tag{71}$$

Letting

$$A=\begin{cases}\frac{1}{4\mu_1\cosh(\pi\varepsilon)}(\text{upper-half plane})\\ \frac{1}{4\mu_2\cosh(\pi\varepsilon)}(\text{lower-half plane})\end{cases}\quad B=\sqrt{\frac{r}{2\pi}} \tag{72}$$

we can now write the gradients of the auxiliary displacements as:

$$u_{x,x}^{(2)}=A\left(Bf_{x,x}+\frac{r_{,x}f_x}{4\pi B}\right),\quad u_{x,y}^{(2)}=A\left(Bf_{x,y}+\frac{r_{,y}f_x}{4\pi B}\right) \tag{73}$$

$$u_{y,x}^{(2)}=A\left(Bf_{y,x}+\frac{r_{,x}f_y}{4\pi B}\right),\quad u_{y,y}^{(2)}=A\left(Bf_{y,y}+\frac{r_{,y}f_y}{4\pi B}\right) \tag{74}$$

and the auxiliary strains can now be evaluated from Eq. (61). Using Hooke's law, the auxiliary stresses are computed from the auxiliary strains.

The contour integral in Eq. (50) is not the best form suited for numerical calculations. We therefore recast the integral into an equivalent domain form by multiplying the integrand

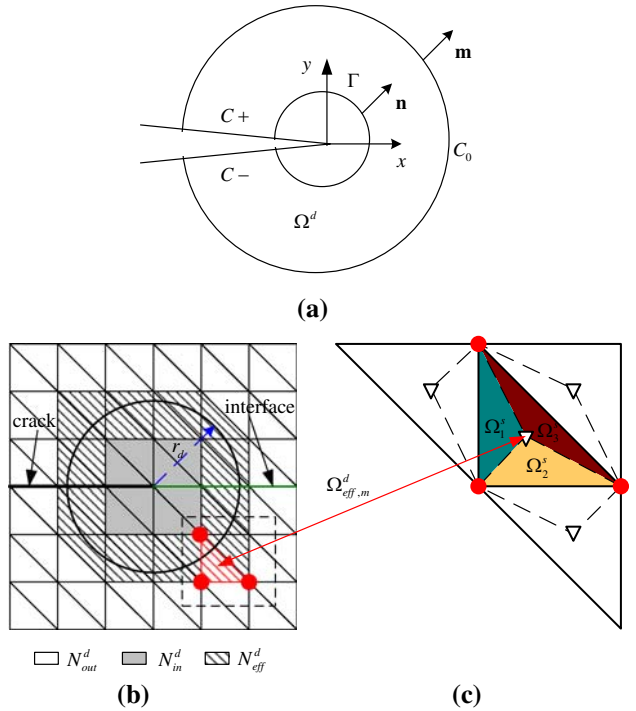

Fig. 6 **a** Conventions at crack tip. Domain Ω^d is enclosed by Γ, C_+, C_- and C_0. Unit normal $m_j = -n_j$ on Γ and $m_j = n_j$ on C_+, C_- and C_0; **b** different types of elements at the crack tip for calculation of the interaction integral; **c** each triangular element domain hosts three sub-parts of smoothing domains associated with three edges, e.g. for element domain $\Omega^d_{eff,m}$, three sub-parts Ω^s_1, Ω^s_2 and Ω^s_3 are involved

by a sufficiently smooth weighting function q which takes a value of unity on an open set containing the crack tip and vanishes on an outer prescribed contour C_0 as shown in Fig. 6a. Assuming the crack faces are traction free, the interaction integral may be written as:

$$I = \int_C \left(\sigma^{(1)}_{ik} \varepsilon^{(2)}_{ik} \delta_{xj} - \sigma^{(1)}_{ij} \frac{\partial u^{(2)}_i}{\partial x} - \sigma^{(2)}_{ij} \frac{\partial u^{(1)}_i}{\partial x} \right) q m_j d\Gamma \quad (75)$$

where the contour $C = \Gamma + C_+ + C_- + C_0$ and m is the unit outward normal to the contour C. Now using the divergence theorem and passing to the limit as the contour Γ is shrunk to the crack tip, we can gives the following equation for the interaction integral in domain form:

$$I = -\int_{\Omega^d} \left(\sigma^{(1)}_{ik} \varepsilon^{(2)}_{ik} \delta_{xj} - \sigma^{(1)}_{ij} \frac{\partial u^{(2)}_i}{\partial x} - \sigma^{(2)}_{ij} \frac{\partial u^{(1)}_i}{\partial x} \right) \frac{\partial q}{\partial x_j} dA \quad (76)$$

where we have used the relations $m_j = -n_j$ on Γ and $m_j = n_j$ on C_+, C_- and C_0.

For the numerical evaluation of the above integral, as shown in Fig. 6b, the domain Ω^d is then set to be the collection of all elements which have a node within a radius of $r_d = r_k h_e$ and this elements set is denoted as N^d. h_e is the characteristic length of an element touched by the crack tip and the quantity is calculated as the square root of the element area.

The weighting function q that appears in the domain form of the interaction integral is set: if a node n_i that is contained in the element $e \in N^d$ lies outside Ω^d, then $q_i = 0$; if node n_i lies in Ω^d, then $q_i = 1$. Since the gradient of q appears in Eq. (76), the elements set N^d_{in} with all the nodes inside Ω^d as shown in Fig. 6b contributes nothing to the interaction integral, and non-zero contribution to the integral is obtained only for elements set N^d_{eff} with an edge that intersects the boundary $\partial\Omega^d$. Therefore, the Eq. (76) can be given by:

$$I = -\sum_{m=1}^{N^d_{eff}} \int_{\Omega^d_{eff,m}} \left(\sigma^{(1)}_{ik} \varepsilon^{(2)}_{ik} \delta_{xj} - \sigma^{(1)}_{ij} \frac{\partial u^{(2)}_i}{\partial x} - \sigma^{(2)}_{ij} \frac{\partial u^{(1)}_i}{\partial x} \right) \frac{\partial q}{\partial x_j} dA \quad (77)$$

where $\Omega^d_{eff,m}$ is domain of the mth element in the elements set N^d_{eff}.

It is noted that each triangular element domain hosts three sub-parts of smoothing domains associated with three edges, e.g. for element domain $\Omega^d_{eff,m}$, three sub-parts Ω^s_1, Ω^s_2 and Ω^s_3 are involved as shown in Fig. 6c. The strains are smoothed and thus constant in each parts belonging to three different smoothing domains. Therefore, the integration in Eq. (77) for one element (e.g. $\Omega^d_{eff,m}$) is conducted by the summation of integration for three sub-parts (Ω^s_1, Ω^s_2 and Ω^s_3).

$$\int_{\Omega^d_{eff,m}} W \frac{\partial q}{\partial x_j} dA = \sum_{n=1}^{3} \int_{\Omega^s_n} W \frac{\partial q}{\partial x_j} dA \quad (78)$$

where

$$W = \sigma^{(1)}_{ik} \varepsilon^{(2)}_{ik} \delta_{xj} - \sigma^{(1)}_{ij} \frac{\partial u^{(2)}_i}{\partial x} - \sigma^{(2)}_{ij} \frac{\partial u^{(1)}_i}{\partial x} \quad (79)$$

6 Numerical examples

6.1 Centre-crack in an infinite bimaterial plate

The problem of an interface crack between two dissimilar elastic semi-infinite planes (Fig. 1) is first studied. The exact solution to this problem under remote traction $\mathbf{t} = \sigma^\infty_{yy} + i\tau^\infty_{xy}$ was obtained by Rice and Sih [6]. The solution for K_I and K_{II} at the right crack tip is [5,6]:

$$\mathbf{K} = K_I + iK_{II} = (\sigma^\infty_{yy} + i\tau^\infty_{xy})(1 + 2i\varepsilon)\sqrt{\pi a}(2a)^{-i\varepsilon} \quad (80)$$

We first consider the case of pure tension remote loading. In the computation, only half of the specimen is considered with the appropriate displacement constraint due to symmetry (Fig. 7). The right edge are constrained in x direction to

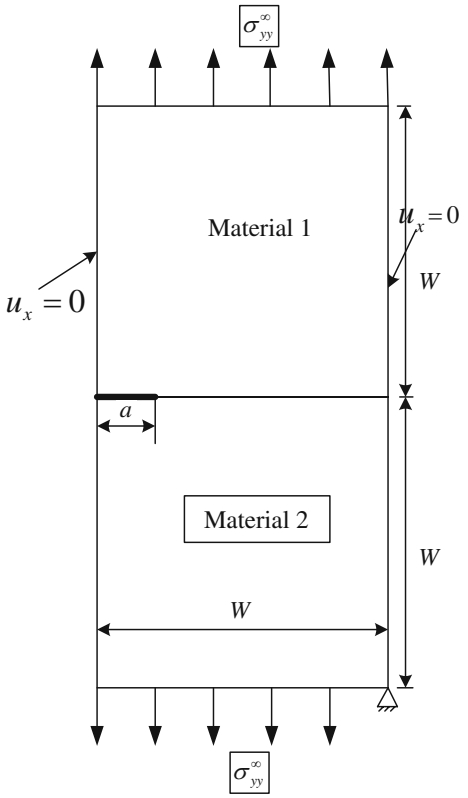

Fig. 7 Centre-crack under remote tension (half model)

remove the edge singularity [6]. The factors K_0 and G_0 are used to normalize the stress intensity factors and the energy release rate, respectively.

$$K_0 = \sigma_{22}^{\infty}\sqrt{\pi a} \quad G_0 = \frac{(\sigma_{22}^{\infty})^2 a}{E_1} \tag{81}$$

where $2a$ is the crack length. The material constants used in the numerical computation are: $E_1 = 1 \times 10^3$, $E_2/E_1 = 22$, $v_1 = 0.3$ and $v_2 = 0.2571$, and plane strain conditions are assumed. The exact solutions from Eq. (80) are:

$$\frac{K_I}{K_0} = 1.008 \quad \frac{K_{II}}{K_0} = 0.1097 \quad \frac{G}{G_0} = 1.4358 \tag{82}$$

The crack dimension is selected as $a = 1$. Since the exact solution is for the infinite domain problem, the sample size $W/a = 30$ is used in all models to avoid the effect of finite size. Five structured meshes with a/h: (3.0, 4.0, 6.0, 8.0 and 10.0) and one unstructured mesh from ABAQUS are adopted, where h is the mesh spacing. A sample structured mesh ($a/h = 8.0$) and unstructured mesh in the vicinity of crack tip are, respectively, shown in Fig. 8a and b. All the studies are conducted using the domain radius parameter $r_k = 4$, unless stated to be otherwise. The strain energy is defined as:

$$\|\mathbf{u}\|_{E(\Omega)} = \left(\frac{1}{2}\int_{\Omega} \boldsymbol{\varepsilon}^T \mathbf{D}\boldsymbol{\varepsilon} \mathrm{d}\Omega\right)^{1/2} \tag{83}$$

6.1.1 *Influence of the number of gauss points*

Table 1 lists the results of the study of the influence of the number of gauss points along one segment of smoothing domains on the SIFs, energy release rate G and strain energy. In this study, the mesh with $a/h = 8.0$ is used. It can be seen that the strain energy and the SIFs keep nearly constant when more than 5 gauss points are used. Thus, all the models discussed later use 5 gauss points along one segment of the smoothing domain. Note that the less the gauss points used, the higher the strain energy and the SIFs. This may be explained that less gauss points bring the effect of the similar reduce integration, and thus lead to over-estimation of results.

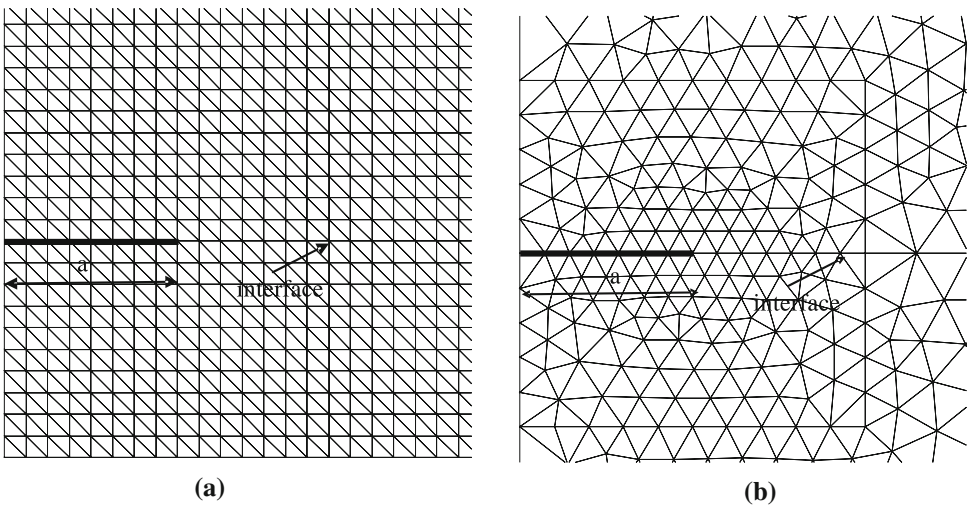

(a) **(b)**

Fig. 8 Meshes in the vicinity of the crack ($a = 1$, $W = 20$), **a** structured mesh with $a/h = 8.0$, **b** unstructured mesh

Table 1 Centre-crack under remote tension: the number of Gauss points effects

N_{gau}	$\|\mathbf{u}\|_{E(\Omega)}$	K_I/K_0 (% error)	K_{II}/K_0 (% error)	G/G_0 (% error)
1	0.01049016	1.0063 (0.1)	0.1100 (0.2)	1.4306 (0.3)
3	0.01048783	1.0060 (0.2)	0.1099 (0.1)	1.4297 (0.4)
5	0.01048779	1.0060 (0.2)	0.1098 (0.1)	1.4297 (0.4)
7	0.01048778	1.0060 (0.2)	0.1098 (0.1)	1.4297 (0.4)

Table 2 Centre-crack under remote tension: comparison of stress intensity factors and energy release rate using the standard FEM, the singular FEM, ES-FEM and the singular ES-FEM

Exact solution	Mesh (a/h)	3.0 (% error)	4.0 (% error)	6.0 (% error)	8.0 (% error)	10.0 (% error)
$K_I/K_0 = 1.008$	FEM	0.9740 (3.4)	0.9834 (2.4)	0.9903 (1.8)	0.9939 (1.4)	0.9959 (1.2)
	Sin FEM*	1.0030 (0.5)	1.0046 (0.4)	1.0057 (0.3)	1.0059 (0.2)	1.0062 (0.2)
	ES-FEM	0.9944 (1.3)	0.9989 (0.9)	1.0020 (0.6)	1.0033 (0.5)	1.0041 (0.4)
	Sin ES-FEM	1.0039 (0.4)	1.0051 (0.3)	1.0060 (0.2)	1.0061 (0.2)	1.0063 (0.2)
$K_{II}/K_0 = 0.1097$	FEM	0.1244 (13.4)	0.1192 (8.6)	0.1141 (4.6)	0.1122 (2.3)	0.1111 (1.3)
	Sin FEM*	0.1119 (2.0)	0.1106 (0.9)	0.1105 (0.9)	0.1101 (0.3)	0.1099 (0.2)
	ES-FEM	0.1165 (6.2)	0.1134 (3.4)	0.1118 (1.0)	0.1108 (1.0)	0.1104 (0.6)
	Sin ES-FEM	0.1114 (1.6)	0.1104 (0.7)	0.1103 (0.6)	0.1100 (0.3)	0.1099 (0.2)
$G/G_0 = 1.4358$	FEM	1.3459 (6.3)	1.3699 (4.6)	1.3872 (3.4)	1.3964 (2.7)	1.4018 (2.4)
	Sin FEM*	1.4219 (1.0)	1.4261 (0.7)	1.4292 (0.5)	1.4296 (0.4)	1.4304 (0.4)
	ES-FEM	1.3993 (2.5)	1.4109 (1.7)	1.4188 (1.2)	1.4223 (0.9)	1.4244 (0.8)
	Sin ES-FEM	1.4244 (0.8)	1.4273 (0.6)	1.4296 (0.4)	1.4301 (0.4)	1.4306 (0.3)

* The singular FEM uses the six-node triangular meshes. However, the comparison in every column is conducted under the meshes with the same DOFs for the purpose of justice

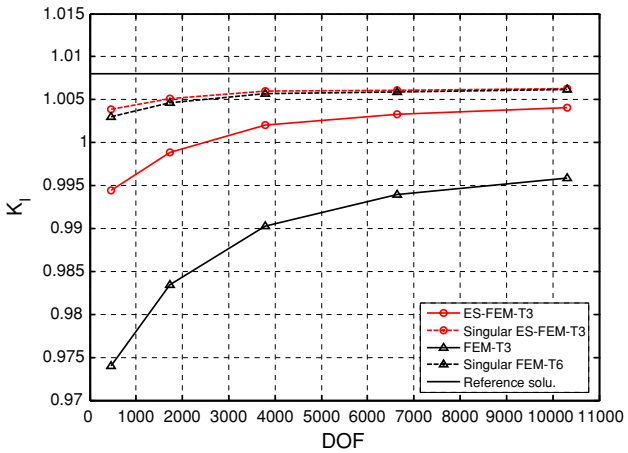

Fig. 9 Convergence of the K_I for Centre-crack under remote tension

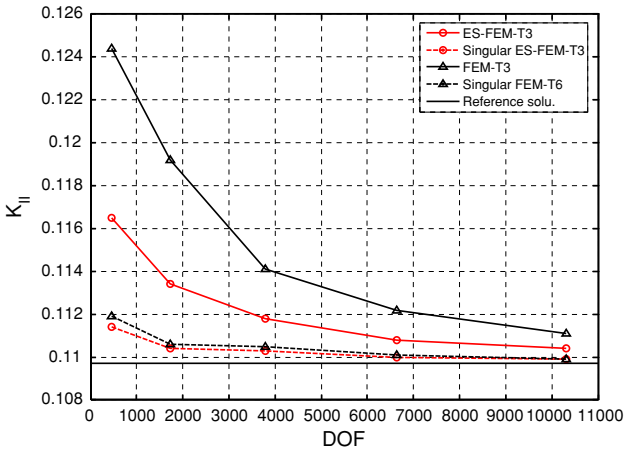

Fig. 10 Convergence of the K_{II} for Centre-crack under remote tension

6.1.2 Accuracy of the SIFs and the energy release rate

In Table 2 and Figs. 9, 10 and 11, the comparison of the SIFs and the energy release rate using different numerical methods (the standard FEM, the singular FEM, ES-FEM, and the singular ES-FEM) is presented. Note that the six-node triangular meshes are used by the singular FEM, and the DOFs of these quadratic meshes are the same as those of the linear meshes other methods use for the purpose of fair comparison. It can be found that the singular ES-FEM improves significantly the accuracy of SIFs and G in comparison with the standard FEM and ES-FEM, no matter the mesh size used. In addition, compared to the singular FEM, the K_I, K_{II} and G of singular ES-FEM are a little closer to the exact values. More importantly, the relative errors of K_I, K_{II} and G using the singular ES-FEM are all within 1 percent for all

Table 3 Centre-crack under remote tension: domain independence study

Mesh	r_k	K_I/K_0 (% error)	K_{II}/K_0 (% error)	G/G_0 (% error)
Structured $a/h_e = 4.0$	2	1.0123 (0.4)	0.1078 (1.7)	1.4467 (0.8)
	3	1.0052 (0.3)	0.1109 (1.1)	1.4276 (0.6)
	4	1.0048 (0.3)	0.1103 (0.6)	1.4262 (0.7)
Structured $a/h_e = 8.0$	2	1.0129 (0.5)	0.1065 (2.9)	1.4480 (0.9)
	3	1.0059 (0.2)	0.1094 (0.3)	1.4291 (0.5)
	4	1.0060 (0.2)	0.1098 (0.1)	1.4297 (0.4)
	5	1.0061 (0.2)	0.1100 (0.3)	1.4293 (0.4)
	6	1.0061 (0.2)	0.1100 (0.3)	1.4295 (0.4)
Unstructured mesh	2	1.0036 (0.4)	0.1095 (0.2)	1.4229 (0.9)
	3	1.0058 (0.2)	0.1099 (0.2)	1.4289 (0.5)
	4	1.0060 (0.2)	0.1099 (0.2)	1.4293 (0.4)
	5	1.0059 (0.2)	0.1098 (0.1)	1.4292 (0.4)

Table 4 Centre-crack under remote tension: robust study

Crack-tip perturbation Δ/a	K_1/K_0 (% error)	K_{II}/K_0 (% error)	G/G_0 (% error)
0	1.0060 (0.2)	0.1098 (0.1)	1.4297 (0.4)
−0.001	1.0055 (0.3)	0.1098 (0.1)	1.4281 (0.5)
0.001	1.0066 (0.1)	0.1099 (0.2)	1.4314 (0.3)

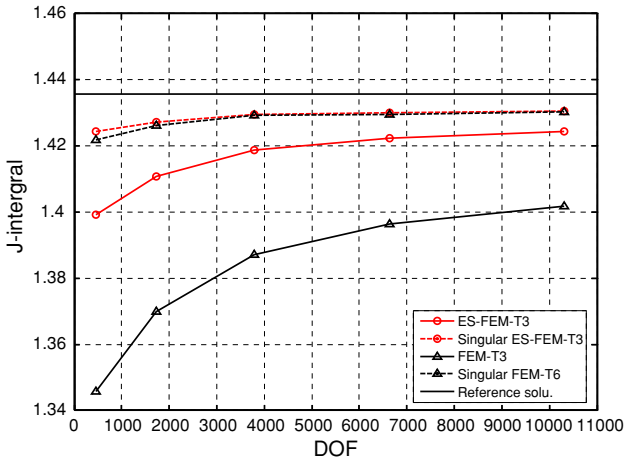

Fig. 11 Convergence of the J-integral for Centre-crack under remote tension

the models used in this study, excepted the case of K_{II} value with the very coarse mesh ($a/h = 3.0$). All of these indicate the singular ES-FEM can solve the interface crack problems effectively.

6.1.3 Domain independence study

Table 3 gives the results of domain independence study using both the structured mesh and unstructured mesh. We can easily observe domain independence of the SIFs for $r_k > 3$ on both structured and unstructured meshes.

6.1.4 Robustness study

To study the robustness of the singular ES-FEM, a simple test is conducted. The crack-tip location is perturbed by $\Delta/a = \pm 0.001$ and the results are compared to those when $\Delta = 0$. The mesh parameter is $a/h = 8.0$. The results are shown in Table 4. From the results, we can notice clearly that the SIFs and G from all the numerical calculations are in excellent agreement with the corresponding exact solutions.

6.1.5 Material mismatch study

To study the performance of the singular ES-FEM on interface cracks for different material property pairs, we varied the ratio E_1/E_2 from 2 to 1,000 with the constant poison ratios: $v_1 = 0.3$ and $v_2 = 0.2571$. It is observed that the results are also accurate to within a few percent relative errors in Table 5, which demonstrates again the effectiveness of the singular ES-FEM for bimaterial interface cracks.

6.1.6 Shear loading condition

Next, we consider the bimaterial plate problem under remote shear tractions. The geometry size, crack configuration and boundary conditions are shown in Fig. 12. In the computation, full model is considered to demonstrate the computational strategy for problems containing more than two crack tips. The same material parameters as before are used in this case: $E_1 = 1 \times 10^3$, $E_2/E_1 = 22$, $v_1 = 0.3$ and $v_2 = 0.2571$,

Table 5 Centre-crack under remote tension: material mismatch study

E_1/E_2	ε	Singular ES-FEM			Exact solution		
		K_I/K_0 (% error)	K_{II}/K_0 (% error)	G/G_0 (% error)	$\frac{K_I}{K_0}$	$\frac{K_{II}}{K_0}$	$\frac{G}{G_0}$
2	0.0249	0.9995 (0.12)	0.0327 (0.64)	2.1497 (0.25)	1.0007	0.0325	2.1551
4	0.0516	1.0016 (0.14)	0.0678 (0.72)	1.7633 (0.29)	1.0030	0.0673	1.7684
8	0.0699	1.0039 (0.17)	0.0915 (0.36)	1.5620 (0.35)	1.0056	0.0912	1.5675
20	0.0833	1.0060 (0.19)	0.1088 (0.16)	1.4375 (0.41)	1.0079	0.1086	1.4434
40	0.0883	1.0072 (0.17)	0.1151 (0.03)	1.3959 (0.39)	1.0089	0.1151	1.4013
100	0.0914	1.0081 (0.14)	0.1192 (0.11)	1.3712 (0.33)	1.0096	0.1191	1.3758
1000	0.0933	1.0089 (0.11)	0.1217 (0.05)	1.3569 (0.26)	1.0100	0.1216	1.3604

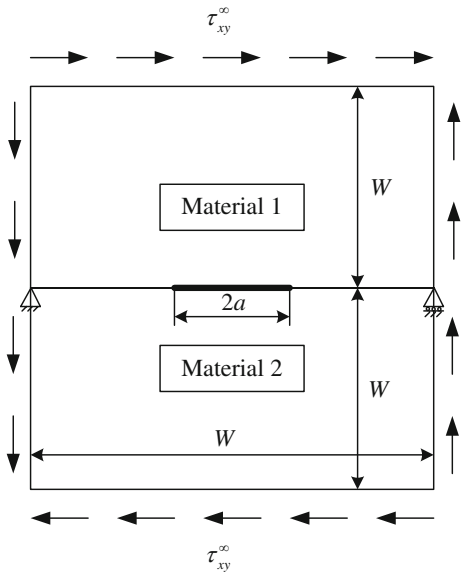

Fig. 12 Centre-crack under remote shear

and plane strain conditions are considered. The exact solution under pure shear loading ($\sigma_{yy}^{\infty} = 0$) is obtained from Eq. (80).

$$K_0 = \tau_{xy}^{\infty}\sqrt{\pi a} \quad G_0 = \frac{(\tau_{xy}^{\infty})^2 a}{E_1} \tag{84}$$

$$\frac{K_I}{K_0} = \pm 0.1097 \quad \frac{K_{II}}{K_0} = 1.008 \quad \frac{G}{G_0} = 1.4358 \tag{85}$$

where K_I is positive at the left crack tip and negative at the right crack tip. The specimen dimensions are set as: $a = 1$ and $W/a = 30$. Here too, five structured meshes with a/h: (3.0, 4.0, 6.0, 8.0 and 10.0) are considered; All the studies, except domain independence study, are conducted using the domain radius parameter $r_k = 4$.

The SIFs and the energy release rate obtained using different numerical methods are compared in Table 6 and Figs. 13, 14 and 15. It can be seen again that the SIFs and the energy release rate of the singular ES-FEM approach the exact solutions much more than that of the standard FEM and ES-FEM,

Table 6 Centre-crack under remote shear: comparison of stress intensity factors and energy release rate using the standard FEM, the singular FEM, ES-FEM and the singular ES-FEM

Exact solution	Mesh (a/h)	3.0 (% error)	4.0 (% error)	6.0 (% error)	8.0 (% error)	10.0 (% error)
$K_I/K_0 = -0.1097$	FEM	−0.1310 (19.4)	−0.1284 (17.0)	−0.1240 (13.0)	−0.1214(10.6)	−0.1196 (9.0)
	Sin FEM*	−0.1109 (1.1)	−0.1108 (1.0)	−0.1105 (0.7)	−0.1104 (0.6)	−0.1103 (0.5)
	ES-FEM	−0.1215 (10.7)	−0.1185 (8.0)	−0.1155 (5.3)	−0.1141 (4.0)	−0.1132 (3.2)
	Sin ES-FEM	−0.1106 (0.8)	−0.1105 (0.7)	−0.1104 (0.6)	−0.1104 (0.6)	−0.1103 (0.5)
$K_{II}/K_0 = 1.008$	FEM	0.9789 (2.9)	0.9823 (2.6)	0.9889 (1.9)	0.9931 (1.5)	0.9957 (1.2)
	Sin FEM*	1.0029 (0.5)	1.0041 (0.4)	1.0057 (0.3)	1.0065 (0.2)	1.0069 (0.1)
	ES-FEM	0.9937 (1.4)	0.9977 (1.0)	1.0015 (0.7)	1.0034 (0.5)	1.0045 (0.4)
	Sin ES-FEM	1.0037 (0.4)	1.0050 (0.3)	1.0062 (0.2)	1.0068 (0.1)	1.0072 (0.1)
$G/G_0 = 1.4358$	FEM	1.3611 (5.2)	1.3693 (4.6)	1.3861 (3.5)	1.3967 (2.7)	1.4034 (2.3)
	Sin FEM*	1.4214 (1.0)	1.4247 (0.8)	1.4292 (0.5)	1.4314 (0.3)	1.4325 (0.2)
	ES-FEM	1.3984 (2.6)	1.4086 (1.9)	1.4184 (1.2)	1.4233 (0.9)	1.4262 (0.7)
	Sin ES-FEM	1.4231 (0.9)	1.4268 (0.6)	1.4301 (0.4)	1.4318 (0.3)	1.4328 (0.2)

* The singular FEM uses the six-node triangular meshes. However, the comparison in every column is conducted under the meshes with the same DOFs

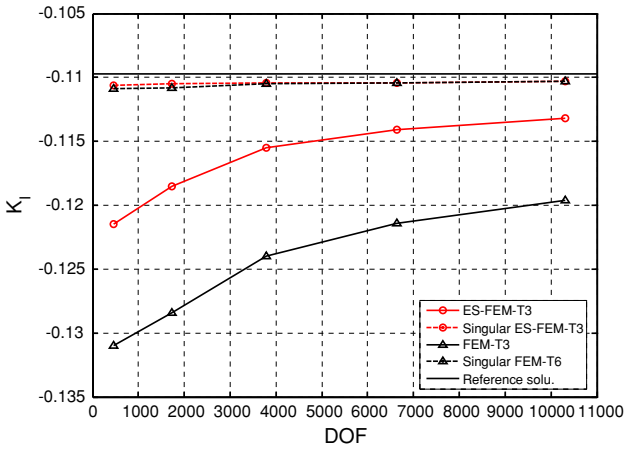

Fig. 13 Convergence of the K_I for centre-crack under remote shear

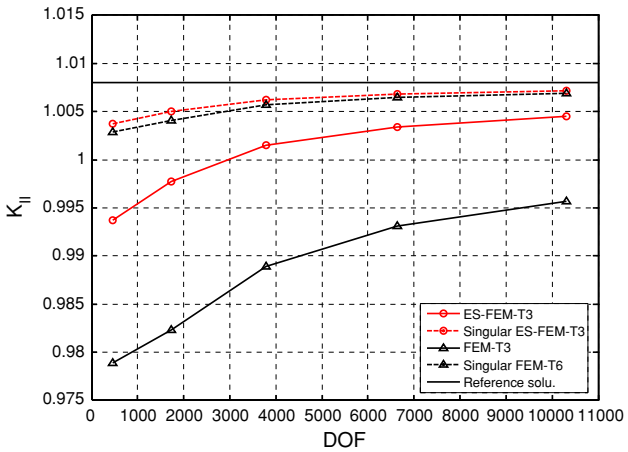

Fig. 14 Convergence of the K_{II} for centre-crack under remote shear

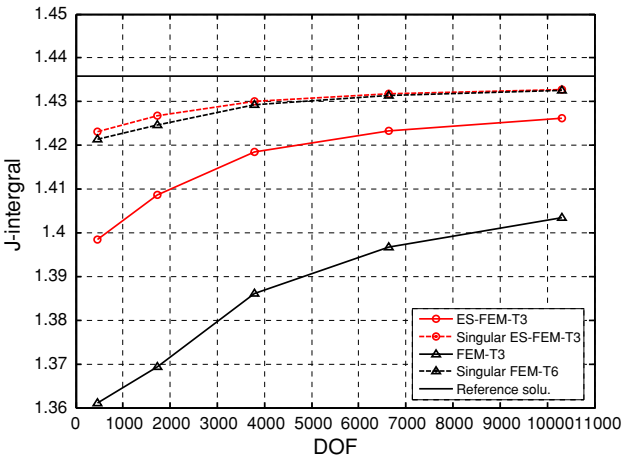

Fig. 15 Convergence of the J-integral for centre-crack under remote shear

Table 7 Centre-crack under remote shear: domain independence study

Crack tip	r_k	K_I/K_0 (% error)	K_{II}/K_0 (% error)	G/G_0 (% error)
Left	2	0.1051 (4.26)	1.0085 (0.1)	4.2619 (0.1)
	3	0.1098 (0.04)	1.0051 (0.3)	1.4267 (0.6)
	4	0.1098 (0.08)	1.0054 (0.3)	1.4275 (0.6)
	5	0.1098 (0.06)	1.0053 (0.3)	1.4274 (0.6)
Right	2	−0.1099 (0.1)	1.0122 (0.4)	1.4467 (0.8)
	3	−0.1095 (0.2)	1.0073 (0.1)	1.4329 (0.2)
	4	−0.1104 (0.6)	1.0068 (0.1)	1.4318 (0.3)
	5	−0.1103 (0.5)	1.0067 (0.1)	1.4315 (0.3)

at the mesh with the same DOFs. Also, the K_I, K_{II} and G of singular ES-FEM are a little closer to the exact values than those of singular FEM. Moreover, the maximum relative error of all these values obtained by the singular ES-FEM is only 1.1% even at the relative coarse mesh.

In Table 7, domain independency in the SIFs using the singular ES-FEM is also studied for this shear loading. We can observe domain independence of the SIFs at both the left and right crack tip for $r_k > 3$. Again, the singular ES-FEM results are found to be in good agreement with the reference solutions. Results of the material mismatch study are also conducted and given in Table 8. Excellent agreement between the normalized K_I, K_{II} and G computed by the singular ES-FEM and the exact correspondence is realized for a wide range of material combinations ($E_1/E_2 = 2 \sim 1000$).

6.2 Film/substrate system by the four point bending test

The second example is a film/substrate system with the four point bending test. Owing to symmetry, one half of the specimen is used in the computation. The specimen dimensions, crack orientation, loading and the displacement boundary conditions are given in Fig. 16. The thickness of film is h_f and that of the substrate is h_s, with the total thickness denoted by h_t. E_f and v_f are used to denote Young's modulus and Poisson's ratio of film. E_s and v_s are the corresponding properties for the substrate.

When the interface crack length significantly exceeds the thickness of the film, steady state conditions are reached and the energy release rate stabilizes to a constant value, G_{ss}, the steady state energy [32]:

$$G_{ss} = \frac{3(1-v_s^2)P^2L^2}{2E_s b^2 h_t^3}\left\{\left(\frac{h_t}{h_s}\right)^3 - \lambda\left[\left(\frac{h_f}{h_t}\right)^3 + \lambda\left(\frac{h_s}{h_t}\right)^3 + 3\lambda\frac{h_f h_s}{h_t^2}\left(\frac{h_f}{h_t} + \lambda\frac{h_s}{h_t}\right)\right]\right\} \tag{86}$$

where b is the depth of film/substrate system, $P = 1$ is the point load applied at the right-top corner as shown in Fig. 16 and λ is defined as:

$$\lambda = \frac{E_s(1-v_f^2)}{E_f(1-v_s^2)} \tag{87}$$

Table 8 Centre-crack under remote shear: material mismatch study*

E_1/E_2	ε	Singular ES-FEM			Exact solution		
		K_I/K_0 (% error)	K_{II}/K_0 (% error)	G/G_0 (% error)	$\frac{K_I}{K_0}$	$\frac{K_{II}}{K_0}$	$\frac{G}{G_0}$
2	0.0249	−0.0318 (2.2)	0.9989 (0.2)	2.1473 (0.4)	−0.0325	1.0007	2.1551
4	0.0516	−0.0671 (0.3)	1.0013 (0.2)	1.7622 (0.4)	−0.0673	1.0030	1.7684
8	0.0699	−0.0916 (0.5)	1.0040 (0.2)	1.5622 (0.3)	−0.0912	1.0056	1.5675
20	0.0833	−0.1092 (0.6)	1.0066 (0.1)	1.4393 (0.3)	−0.1086	1.0079	1.4434
40	0.0883	−0.1157 (0.6)	1.0078 (0.1)	1.3977 (0.2)	−0.1151	1.0089	1.4013
100	0.0914	−0.1199 (0.6)	1.0085 (0.1)	1.3725 (0.2)	−0.1191	1.0096	1.3758
1000	0.0933	−0.1224 (0.6)	1.0090 (0.1)	1.3573 (0.2)	−0.1216	1.0100	1.3604

* The SIFs and the exact energy release rate are from the right crack tip

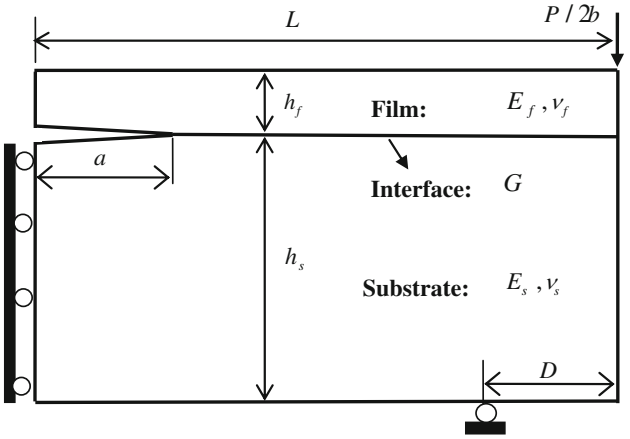

Fig. 16 Schematic-diagram of film/substrate system by four point bending test (half model)

The phase angle is computed by taking the characteristic length l given in Eq. (8) to be the total thickness of film/substrate system h_t:

$$\psi = \tan^{-1}\left(\frac{\mathrm{Im}[\mathbf{K}h_t^{i\varepsilon}]}{\mathrm{Re}[\mathbf{K}h_t^{i\varepsilon}]}\right) \tag{88}$$

In addition, we also choose the factors K_0 and G_0 are used to normalize the SIFs and the energy release rate, respectively.

$$K_0 = \frac{PL}{bh_t^{3/2}} \quad G_0 = \frac{(1-v_s^2)P^2L^2}{E_s b^2 h_t^3} \tag{89}$$

In the numerical model, the depth b is taken to be unity, $h_f = 1, h_t/h_f = 10, L/D = 2.5, D/h_t = 5$ and $a/h_t = 3$. Thus, the problem domain is $L \times h_t = 125 \times 10$ and $a = 30$. The material parameters are $E_s = 1 \times 10^3$, $E_f/E_s = 10$ and $v_f = v_s = 0.3$. Based on this, the exact steady state energy release rate is 1.3632 from Eq. (86). The mesh with $h_t/h = 6.0$ and the domain radius parameter $r_k = 4$ are used. Note that the singular FEM uses the six-node triangular meshes which have the same DOFs as the meshes other methods use. Comparison of energy release rates obtained by the standard FEM, the singular FEM, ES-FEM and the singular ES-FEM are presented in Table 9. Results for K_I, K_{II} and ψ are also indicated for completeness. From the results, it is found again that the singular ES-FEM provide more accuracy of energy release rate compared to the standard FEM, the singular FEM and ES-FEM. Moreover, the energy release rate obtained by the singular ES-FEM is in good agreement with the exact value [32] with a fraction of percent error.

Table 9 Film/substrate system by four point bending test: comparison of stress intensity factors and energy release rate using the standard FEM, the singular FEM, ES-FEM and the singular ES-FEM under the same triangular mesh with $h_t/h = 6.0^+$

Method	K_I/K_0	K_{II}/K_0	ψ	G/G_0 (% error)
FEM	0.9386	1.2832	43.81	1.3142 (3.6)
Sin FEM*	0.9564	1.2965	43.54	1.3502 (0.9)
ES-FEM	0.9517	1.2946	43.68	1.3423 (1.5)
Sin ES-FEM	0.9572	1.2970	43.57	1.3511 (0.8)

$^+$ The exact energy release rate from Eq. (86) is 1.3632.
* The singular FEM uses the six-node triangular mesh which has the same DOFs as the mesh other methods use

Then, the fixed total thickness $h_t = 10$ is used and the thickness ratio h_f/h_t is varied from 0.1 to 0.5. Also, we varied the material properties combinations of film and substrate. Table 10 lists the steady state energy release rate for different thickness ratio and different material combinations. Again, we can observe that all the results by the singular ES-FEM are in excellent agreement with the corresponding reference solutions, and the relative errors are less than 1%.

7 Conclusion

In this work, a singular edge-based smoothed finite element method (ES-FEM) is proposed to solve problems with mix-mode interface cracks between two dissimilar isotropic

Table 10 Film/substrate system by four point bending test: effect of thickness ratio

$\frac{E_f}{E_s}$	$\frac{h_f}{h_s+h_f}$	Singular ES-FEM				Exact solution
		K_I/K_0	K_{II}/K_0	ψ	G/G_0 (% error)	$\frac{G}{G_0}$
10	0.1	0.9572	1.2970	43.57	1.3511 (0.8)	1.3632
	0.2	1.2948	1.6356	41.63	2.2626 (0.7)	2.2793
	0.3	1.7766	1.9884	38.22	3.6969 (0.7)	3.7254
	0.4	2.4676	2.4454	34.74	6.2754 (0.8)	6.3249
	0.5	3.4789	3.1173	31.86	11.3451 (0.9)	11.4523
0.1	0.1	0.0729	0.1000	63.90	0.0801 (0.9)	0.0807
	0.2	0.1618	0.1787	57.85	0.3022 (0.7)	0.3043
	0.3	0.3024	0.2844	53.25	0.8959 (0.5)	0.9010
	0.4	0.5295	0.4372	49.55	2.4518 (0.5)	2.4655
	0.5	0.8949	0.6661	46.66	6.4706 (0.8)	6.5228

materials. A five-node singular element is designed within the framework of ES-FEM to construct the singular shape functions. To model the oscillatory effect $r^{i\varepsilon}$ at the crack tip, the mix-mode stress intensity factors are numerically extracted by the domain form of the interaction integral with appropriate modifications. Through the formulation and numerical examples, some conclusions can be drawn as follows:

1. In the Gauss integrations for computing the stiffness matrix, at least 5 gauss points should be used along one segment of the crack tip smoothing domain for the five-node singular element to ensure the accuracy of results.
2. Domain independence of the SIFs are observed for the domain radius parameter $r_k > 3$, regardless of one crack tip or multiple crack tips considered in the computation.
3. The singular ES-FEM improves the accuracy of stress intensity factors and energy release rate in comparison with the standard FEM, the singular FEM and ES-FEM.
4. Excellent agreement between the numerical results and reference solutions with less than 1% relative error was realized for a wide range of material combinations and boundary conditions. This indicates that the singular ES-FEM can solve the interface crack problems effectively.

References

1. Yeap KB, Zeng KY, Chi DZ (2008) Determining the interfacial toughness of low-k films on Si substrate by wedge indentation: further studies. Acta Mater 56:977–984
2. Hutchinson JW, Suo Z (1992) Mixed mode cracking in layered materials. In: Hutchinson JW, Wu TY (eds) Advances in applied mechanics, pp 63–191
3. Williams ML (1959) The stress around a fault or crack in dissimilar media. Bullet Seismol Soc Am 49:199–204
4. England AH (1965) A crack between dissimilar media. J Appl Mech 32:400–402
5. Rice JR, Sih GC (1965) Plane problems of cracks in dissimilar media. J Appl Mech 32:418–423
6. Rice JR (1988) Elastic fracture mechanics concepts for interfacial cracks. J Appl Mech 55:98–103
7. Henshell RD, Shaw KG (1975) Crack tip finite elements are unnecessary. Int J Numer Methods Eng 9:495–507
8. Barsoum RS (1976) On the use of isoparametric finite elements in linear fracture mechanics. Int J Numer Methods Eng 10:551–564
9. Barsoum RS (1977) Triangular quarter-point elements as elastic and perfectly-plastic crack tip elements. Int J Numer Methods Eng 11:85–98
10. Shih CF, Asaro RJ (1988) Elastic-plastic analysis of cracks on bimaterial interfaces: part I-small scale yielding. J Appl Mech 55:299–316
11. Matos PPL, McMeeking RM, Charalambides PG, Drory MD (1989) A method for calculating stress intensities in bimaterial fracture. Int J Fract 40:235–254
12. Nahta R, Moran B (1993) Domain integrals for axisymmetric interface crack problems. Int J Solids Struct 30(15):2027–2040
13. Belytschko T, Black T (1999) Elastic crack growth in finite elements with minimal remeshing. Int J Numer Methods Eng 45(5):601–620
14. Moes N, Dolbow J, Belytschko T (1999) A finite element method for crack growth without remeshing. Int J Numer Methods Eng 46(1):131–150
15. Belytschko T, Moes N, Usui S, Parimi C (2001) Arbitrary discontinuities in finite elements. Int J Numer Methods Eng 50(4):993–1013
16. Sukumar N, Huang ZY, Prévost JH, Suo Z (2004) Partition of unity enrichment for bimaterial interface cracks. Int J Numer Methods Eng 59:1075–1102
17. Chen JS, Wu CT, Yoon Y (2001) A stabilized conforming nodal integration for Galerkin mesh-free methods. Int J Numer Methods Eng 50:435–466
18. Liu GR, Dai KY, Nguyen TT (2007) A smoothed finite element method for mechanics problems. Comput Mech 39:859–877
19. Liu GR, Nguyen TT, Dai KY, Lam KY (2007) Theoretical aspects of the smoothed finite element method (SFEM). Int J Numer Methods Eng 71:902–930
20. Liu GR, Nguyen-Thoi T, Lam KY (2008) A node-based smoothed finite element method for upper bound solution to solid problems (NS-FEM). Comput Struct 87:14–26
21. Dohrmann CR, Heinstein MW, Jung J, Key SW, Witkowski WR (2000) Node-based uniform strain elements for three-node triangular and four-node tetrahedral meshes. Int J Numer Methods Eng 47:1549–1568

22. Liu GR, Zhang GY, Dai KY, Wang YY, Zhong ZH, Li GY. Han X (2005) A linearly conforming point interpolation method (LC-PIM) for 2D solid mechanics problems. Int J Comput Methods 2(4):645–665
23. Liu GR, Nguyen-Thoi T, Lam KY (2009) An edge-based smoothed finite element method (ES-FEM) for static, free and forced vibration analysis. J Sound Vib 320:1100–1130
24. Nguyen-Thoi T, Liu GR, Lam KY (2009) A face-based smoothed finite element method (FS-FEM) for 3D linear and nonlinear solid mechanics problems using 4-node tetrahedral elements. Int J Numer Methods Eng 78:324–353
25. Liu GR, Gu YT (2001) A point interpolation method for two-dimensional solids. Int J Numer Methods Eng 50:937–951
26. Liu GR, Zhang GY (2008) Edge-based smoothed point interpolation methods. Int J Comput Methods 5:621–646
27. Chen L, Nguyen-Xuan H, Nguyen-Thoi T, Zeng KY, Wu SC (2009) Assessment of smoothed point interpolation methods for elastic mechanics. Commu Numer Methods Eng doi:10.1002/cnm.1251
28. Shih CF (1988) Cracks on bimaterial interfaces: elasticity and plasticity aspects. Mater Sci Eng A 143:77–90
29. Dundurs J (1969) Edge-bonded dissimilar orthogonal elastic wedges. J Appl Mech 36:650–652
30. Moran B, Shih CF (1987) Crack tip and associated domain integrals from momentum and energy balance. Eng Fract Mech 27(6):615–641
31. Li FZ, Shih CF, Needleman A (1985) A comparison of methods for calculating energy release rates. Eng Fract Mech 21(2):405–421
32. Charalambides PG, Lund J, Evans AG, McMeeking RM (1989) A test specimen for determining the fracture resistance of bimaterial interfaces. J Appl Mech 56:77–82